ELSEVIER

Journal of Power Sources 69 (1997) 1–9

JOURNAL OF POWER SOURCES

The benefit of solid oxide fuel cells with integrated air pre-heater

P. Costamagna *

ISTIC, Istituto di Ingegneria Chimica e di Processo 'G.B. Bonino', Facoltà di Ingegneria, Università degli Studi di Genova, via Opera Pia 15, 16145 Genova, Italy

Received 22 November 1995; revised 29 January 1996

Abstract

A new design has recently been proposed in the field of solid oxide fuel cells, consisting of a traditional electrochemical cell integrated with a pre-heater. In this paper a simulation model for the rectangular planar solid oxide fuel cell with integrated air pre-heater is presented. A two-dimensional stack simulation is presented as well, one axis coincides with the fuel flow direction, the other with the stack height. Local quantities such as current density, gas and solid temperatures are reported and cell characteristics predicted. In a parameter study, effects of oxygen utilisation and heat-transfer conditions in the pre-heater on the local temperature distribution of the solid structure are considered. As a result, the benefit of the new cell design becomes evident when low air flow rates are applied. A further advantage associated with the reduced flow rate is the low air temperature at the inlet. © 1997 Elsevier Science S.A.

Keywords: Solid oxide fuel cells; Simulation; Integrated air pre-heater

1. Introduction

Ceramic materials of a solid oxide fuel cell (SOFC) [1], i.e. anode, cathode and electrolyte, cannot withstand steep temperature gradients. Thus, in order to obtain an almost uniform temperature distribution on the cell plane, a higher air-flow rate than that required for fuel oxidation must be fed to the cell at high temperature. As a consequence the air pre-heater and the air blower become the most expensive components of the whole fuel cell plant: for example, they account for about 65% to the investment cost [2] when external methane–steam reforming is applied.

In order to overcome this problem a rectangular SOFC with integrated air pre-heater has recently been proposed by KFA Jülich [3]. A circular shape for the cell and the stack with integrated air pre-heater has been proposed by others [4], and will not be considered here.

The basic idea of this design is to shift the temperature gradient $T_{out} - T_{in}$ from the air channels of a conventional cell to the air flowing into the integrated heat exchanger. Thus, the air-inlet temperature could be reduced by the same amount, or even more if the air-mass flow is decreased.

The heat-exchanger integrated stack is formed by a series of repeat modules, each of them constituted of a traditional planar electrochemical cell coupled with a heat-exchanging element. A detailed design of the traditional planar cell, showing more details such as the gas channels that distribute fuel and oxidant on the cell, can be found elsewhere [1]. A sketch of a rectangular heat-exchanging element is shown in Fig. 1(a): it is a void chamber where the air flows before entering the cathodic compartment of the electrochemical cell. No channels are present. Finally, a scheme of the rectangular stack is presented in Fig. 1(b).

A further proposal of innovation that will be discussed in the present paper is the use of metallic materials instead of ceramic components for the interconnector and for the integrated heat exchanger.

The fuel (pure hydrogen) and the cathodic air stream are in co-flow, whereas the air is pre-heated in counter-flow to the cathodic air. Before entering the fuel cell fresh air passes into the afterburner compartment. Here, the fuel not converted in the cell is burnt to contribute to the air pre-heating. In this way the fuel utilisation is closely related to the air excess and therefore subject to optimisation procedures.

Previous types of SOFC simulation models [5–17] have to be extended to account for the additional internal heat-transfer process in the integrated heat exchanger. In the present work a model accounting for the presence of the integrated heat exchanger is discussed and on this basis a new simulation code is presented in application to a rectangular single cell and to a stack as well. Computational results are discussed and the benefit of this new design is pointed out.

* Corresponding author: Tel.: +39-10-353.2589; Fax: +39-10-353.2586.

PII S0378-7753(96)02386-5

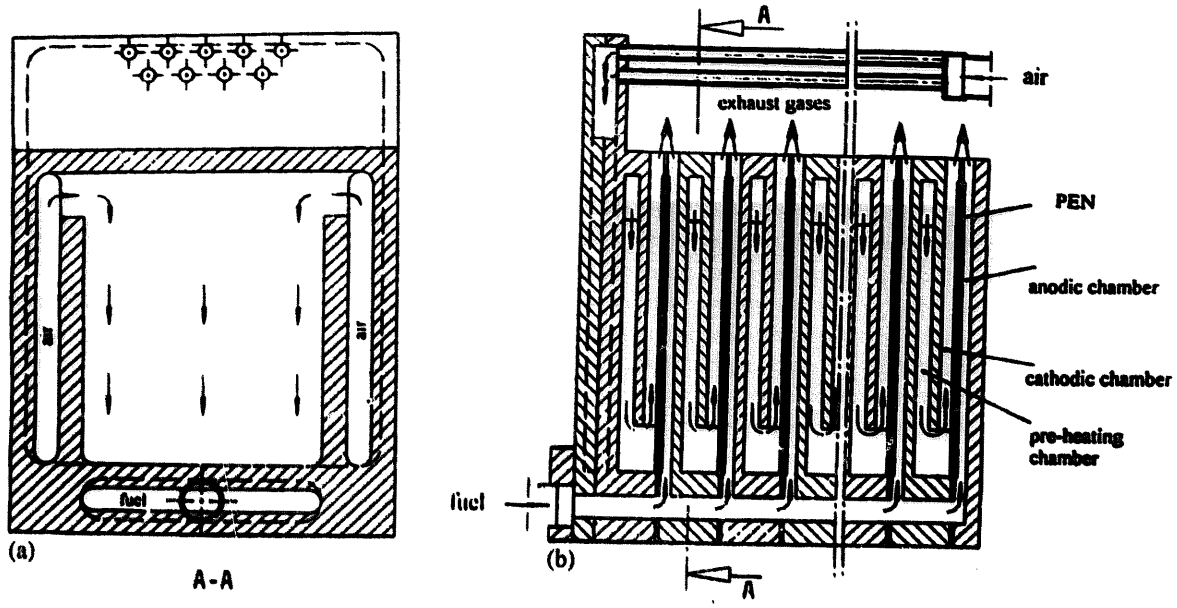

Fig. 1. (a) View of the integrated heat-exchanger plate. (b) Drawing of the stack [3].

2. Simulation model

2.1. Hypotheses of the model and input data

The present stack simulation program is two-dimensional in space and is time-dependent. The length co-ordinate, x, is parallel to the fuel stream direction, the origin coincident with the point where the fuel enters the cell. The z-coordinate is perpendicular to the cell plane. A one-dimensional model of stacked cells is allowed because co- or counter-flow occurs. This implies, however, that the outer stack surfaces in the x–z plane must be considered adiabatic. The remaining surfaces are allowed to radiate or convey heat to the surrounding shell which is assumed to have a uniform and constant temperature.

As the current collectors have a very high electric conductivity, they can be considered as equipotential plates.

The following quantities are required as input data:

1. *Design parameters*: (i) size and configuration of the electrolyte, electrodes, interconnector, heat-exchanger plate; (ii) size and number of gas channels; (iii) number of cells.
2. *Operating conditions*: (i) pressure, inlet temperature, composition and utilisation of the anodic and cathodic gases; (ii) shell temperature; (iii) average current density or cell voltage.
3. *Properties and empirical data*: (i) definition of the materials used; (ii) empirical parameters for the rate-limiting kinetics.

The main output quantities are: (1) electrical power and efficiency; (2) local distributions of current density, gases and solid temperatures, gas compositions and flowrates.

2.2. Balance equations

2.2.1. Simplifications

As already discussed in Refs. [10,16] the heat and mass transfer in the gas channels can be treated as being one-dimensional without undergoing considerable errors. Furthermore, the streamwise diffusion terms can be neglected since the convective mass and heat fluxes are the prevailing contributions. Thus, the mass and energy balances of the gas phase can be written in plug-flow form.

The streamwise molar flux gradient is merely depending on the conversion rates. Similarly the streamwise temperature distribution is determined by the convective heat transfer from the channel walls, while the solid temperature depends on the reaction enthalpies and on the convective heat exchange with the gases.

2.2.2. Mass balance

Under the assumptions made, the mass balance can be written as

$$\frac{\partial n_i}{\partial x} = r_i \tag{1}$$

where i denotes the particular gas component converted.

The reaction rate can be calculated by means of Faraday's law

$$r_i = \nu_i \frac{I}{neF} \tag{2}$$

where ne is the number of electrons transferred in the electrochemical reaction and ν is the stoichiometric factor of the reacting component; ν is negative for reactants and positive

for products. In the case of a cell fed with hydrogen ne is equal to 2, corresponding to the following reactions:

$1/2O_2 + 2e^- \rightarrow O^{2-}$ cathodic reaction
$H_2 + O^{2-} \rightarrow H_2O + 2e^-$ anodic reaction
$H_2 + 1/2O_2 \rightarrow H_2O$ over-all reaction

2.2.3. Energy balance of the gaseous phase

As mentioned above, the streamwise temperature gradient in the gas flows is assumed to depend only on the convection phenomenon due to both the heat and the mass transfer from the channel walls to the bulk of gases

$$\sum_i n_i c_{p,i} \frac{\partial T_g}{\partial x} + \sum_i c_{p,i} \frac{\partial n_i}{\partial x}(T_g - T_s) + h_g B_g \frac{1}{a}(T_g - T_s) = 0 \quad (3)$$

where B is the ratio between the gas–solid heat-exchange area and the cell area, h the heat-transfer coefficient calculated from the Nusselt number, Nu

$$h = Nu \frac{k}{d_h} \quad (4)$$

The value of the Nusselt number generally depends on the channel geometry, the Reynolds number, Re, and the Prandtl number, Pr. For the laminar established flow, however, which holds for the fuel cell channels the Nusselt number is a constant.

Eq. (3) is also applied to the flow through the heat-exchanger section. In this case, of course, the conversion term vanishes.

2.2.4. Energy balance of the solid structure

The energy balance of the solid material describes the unsteady heat conduction in the quasi-homogeneous solid structure of the stack. The convective heat, transferred from the gas flow to the solid, and the reaction enthalpies occur as source terms

$$\frac{1}{s}\sum_g h_g G_g (T_g - T_s) - \frac{1}{s}\left(\frac{\Delta H}{neF} + V\right) I + K_x \frac{\partial^2 T_s}{\partial x^2} + K_z \frac{\partial^2 T_s}{\partial z^2} = \rho_s C_{p,s} \frac{\partial T_s}{\partial t} \quad (5)$$

where K_x and K_z are the effective thermal conductivities of the solid structure, taking the particular cell configurations in both directions into account. In the x-direction parallel heat conduction through the h parallel layers is assumed

$$K_x = \frac{\sum_h K_h \delta_h}{\sum_h \delta_h} \quad (6)$$

while for the z-direction the heat conduction is in series

$$K_z = \frac{\sum_h \delta_h}{\sum_h \frac{\delta_h}{K_h}} \quad (7)$$

In both effective conductivities the contributions of the gas layers are also included.

2.3. Local reaction rate

The internal electric resistance of the cell has been determined according to the procedure proposed by Refs. [5,10,17,18].

In particular, the open-circuit voltage V^{oc} is given by Nernst's equation applied to the over-all reaction

$$V^{oc} = \frac{-\Delta G}{neF} = \frac{-\Delta G^0}{neF} - \frac{RT_s}{neF} \ln\left(\prod_i p_i^{\nu_i}\right) \quad (8)$$

Ionic resistance of the electrolyte, ohmic losses of the electrodes and of the bipolar plate and finally contact resistances have been considered. All quantities except contact resistances are expressed by temperature dependent equation:

$$\frac{1}{R_{el}} = \frac{\beta_1}{T_s^{\beta_2}} \exp\left(-\frac{\beta_3}{T_s}\right) \quad (9)$$

Concentration polarization is usually negligible for SOFC devices, while activation polarization at the anode and cathode electrodes has been considered, according to the equations:

$$\frac{1}{R_{pol,an}} = \frac{neF}{RT_s}\gamma_{1,an}\left(\frac{P_{H_2}}{P_{ref}}\right)^{\gamma 2,an} \exp\left(-\frac{E_{an}}{RT_s}\right) \quad (10)$$

$$\frac{1}{R_{pol,ca}} = \frac{2neF}{RT_s}\gamma_{1,ca}\left(\frac{P_{O_2}}{P_{ref}}\right)^{\gamma 2,ca} \exp\left(-\frac{E_{ca}}{RT_s}\right) \quad (11)$$

So, the potential between the current collectors is given by

$$V^{cc} = V^{oc} - V^{ohm} - V^{pol} \quad (12)$$

where V^{cc} is the voltage at the current collectors, V^{ohm} and V^{pol} are the voltage drops due to ohmic and polarisation effects, respectively.

2.4. Boundary conditions

As shown in Fig. 1 the exhaust anode gas is burnt together with the cathodic off-gas in a separate compartment containing the after-burner heat exchanger which pre-heats the ambient air up to the inlet temperature of the integrated pre-heater. Heat is allowed to be exchanged by convection and radiation from the stack to this region. As a simple assumption the temperature of this compartment is considered to be uniform.

The heat transferred to the stack by convection is given by

$$q = \alpha(T_{shell} - T_s) \quad (13)$$

The radiative contribution is approximated by

$$q = 4e\sigma\left(\frac{T_{shell} + T_s}{2}\right)^3 (T_{shell} - T_s) \quad (14)$$

Because the heat-transfer problem is treated one-dimensionally in each z-plane, the side walls must be considered adiabatic.

2.5. Numerical integration

The balance Eqs. (1), (3) and (5) have to be solved for two spatial coordinates and one temporal one. In fact, however, it is sufficient to treat only Eq. (5) as time-dependent, since mass transfer and all chemical and fluid dynamics processes are fast compared with the heat dispersion in the solid structure. Thus, a steady-state solution of the mass and energy balances of the gaseous phase is found at each time step. Successively a new solid-temperature distribution is calculated using the source terms of the preceding time step.

The integration is performed by applying finite differencing. Fast convergence for the solution of Eq. (5) is achieved by means of the successive overrelaxation method (SOR). The corresponding SOR factor was automatically adjusted during the running of the program, proportionally to the distance from the final solution.

In particular, the following procedure was applied to solve the equations for the single cell:

1. specify the operating conditions in the input file and set an initial solid-temperature distribution;
2. calculate the current density and solve the mass balance;
3. solve the energy balance of the gaseous phase to determine the temperature distribution along the gas channels, and
4. solve the energy balance of the solid to find a new temperature field.

Steps 1 through 4 are repeated until the steady-state solution is reached within a given threshold of accuracy.

The calculation of the whole stack starts from the solution of the single cell. The computation proceeds as follows:

1. extend the results of the single cell to the whole stack;
2. solve mass and energy balances of the gas flow for each cell, and
3. solve the energy balance of the solid, accounting for the outer boundary conditions.

Repeat steps 2 and 3 until the steady-state solution is reached within the accuracy required.

The average temperature level of the solid material is an important design quantity. Since it strongly depends on the inlet temperature and mass flow of the air, an iteration step seems to be useful to find out the solution satisfying the average required value of the solid temperature. For this purpose a PID controller (proportional, integral, differential) for the air-inlet temperature is simulated. Starting from an estimated temperature field of the solid, the temperature of the inlet air is varied proportionally, integrally and differentially to the difference between the actual average temperature of the solid and the target value.

The computer code has been applied to a single adiabatic cell and a stack consisting of five cells. For each computation presented in this paper an average solid temperature of $T_{av} = 1193$ K was required which results in different air-inlet temperatures at the integrated heat exchanger.

3. Computational results

3.1. The single adiabatic cell

Figs. 2 and 3 show the temperature distributions of the fuel, of the air and of the solid structure along a cell operating at an average current density of $j = 3000$ A m^{-2}. The fuel is hydrogen, 80% of which is utilised. The stoichiometry factor of the air flow is $\lambda = 2.7$ resulting in an O_2 utilisation of $U_{O_2} = 0.3$. Further design and operating data are listed in Table 1.

Fig. 2 represents the temperature distribution of the fuel, of the cathodic air and of the air in the integrated heat exchanger along the cell. To come out with an average solid temperature of $T_{s,av} = 1193$ K the air has to enter the stack with a temperature of $T_{air,in} = 710$ K. The air stream running in counter-flow to the cathodic air is continuously heated up by the waste heat electrochemically produced. The temperature of the cathodic and the anodic gases are close to that of the solid material.

Fig. 3 exhibits the solid-structure temperature in a more expanded scale. The maximum temperature is about

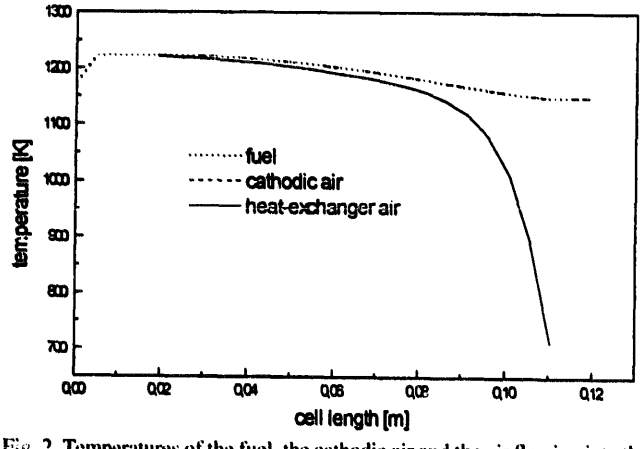

Fig. 2. Temperatures of the fuel, the cathodic air and the air flowing into the integrated heat-exchanger plate along the cell length.

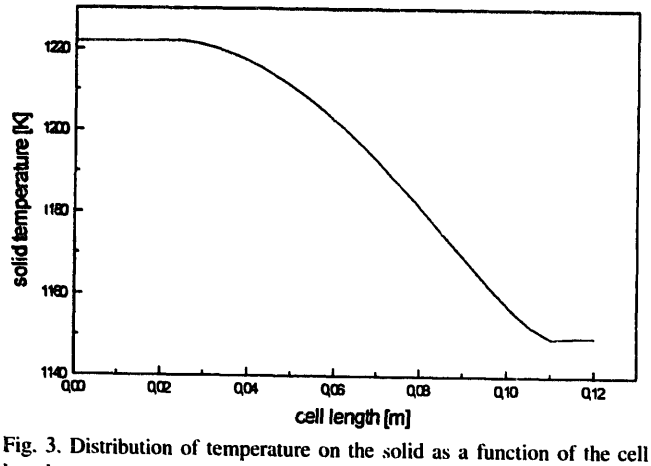

Fig. 3. Distribution of temperature on the solid as a function of the cell length.

Table 1
Design parameters and operating conditions for the simulated rectangular single cell

Simulated rectangular cell	
Design parameters	
Overall cell dimensions	0.12 m×0.1 m
Active cell area	0.01 m^2
Anode, cathode, electrolyte thickness	1×10^{-4} m
Heat-exchanger plate thickness	5×10^{-3} m
Interconnector thickness	2.4×10^{-3} m
Anodic/cathodic channel shape	square
Channel dimension	1×10^{-3} m
Rib dimension	1×10^{-3} m
Operating conditions	
Current density	3000 A m^{-2}
Cell voltage	0.71 V
Pressure	1.013×10^5 Pa
Anodic inlet temperature	1173 K
Cathodic inlet temperature	711 K
Average solid temperature	1193 K
Anodic inlet composition	97% H_2 + 3% H_2O
Cathodic inlet composition	air
Hydrogen-utilisation factor	0.8
Oxygen-utilisation factor	0.3
Heat exchange	adiabatic conditions

$T_s = 1220$ K and the difference observed across the cell is about $\Delta T_s = 70$ K which is a small value with a view to the low air stoichiometry factor of $\lambda = 2.7$.

Due to the low mass flux the high thermal conductivity of the solid material contributes considerably to removal of heat from the entrance region of the cell to the exit where the heat is released to the refrigerant air. Then the heat removal from areas of high waste heat production is not predominantly done by convection, while the heat conduction through the solid structure becomes the prevailing mechanism.

The local current-density distribution is displayed in Fig. 4. As a result of the high fuel utilisation the data vary in a wide range from about 7000 A m^{-2} at the entrance to 1200 A m^{-2} at the outlet. With decreasing utilisation, of course, the uniformity would improve.

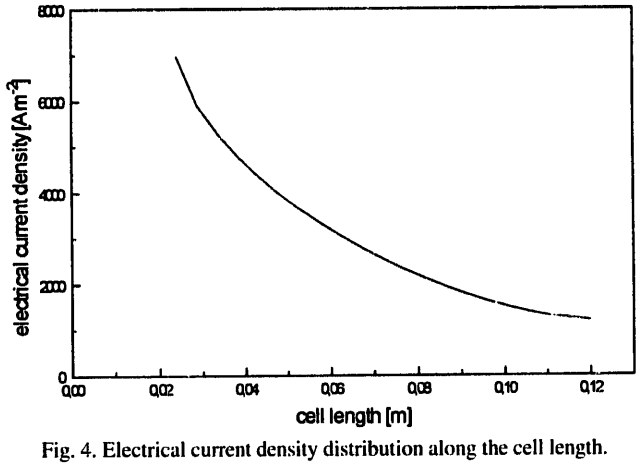

Fig. 4. Electrical current density distribution along the cell length.

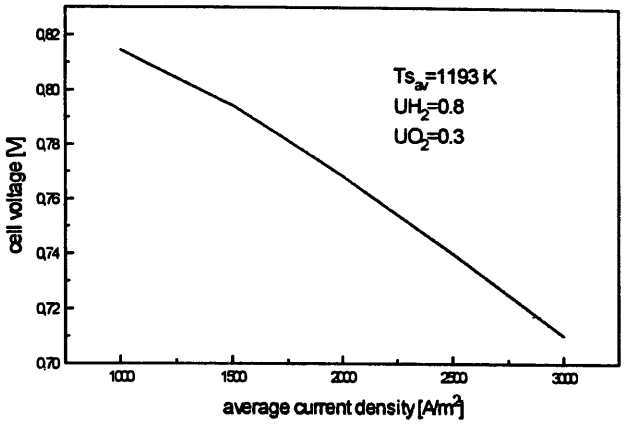

Fig. 5. Characteristic curve for the single cell.

In Fig. 5 the characteristic curve of the adiabatic single cell is reported. The average cell temperature is kept constant, but different solid temperature distributions arise at different operating conditions. Small variations of the cell resistance take place and cause small changes of the line slope, which, anyway, is very similar to a typical SOFC straight line, the voltage of the cell ranging from 0.71 V at 3000 A m^{-2} to 0.81 V at 1000 A m^{-2}.

In a conventional cell built with ceramic materials and not equipped with an integrated heat exchanger maximum solid- and gas-outlet temperatures of $T_s = 1370$ K would occur, even if the inlet air temperature is reduced to 985 K. The corresponding minimum solid temperature is $T_s = 1060$ K, as shown in Fig. 6. The improvements due to the use of metallic interconnectors are pointed out.

Fig. 7 shows how the heat-transfer conditions in the integrated heat exchanger affect the solid temperature distribution. If the label '1' in Fig. 7 stands for the heat-transfer coefficient calculated on the basis of the data reported in Table 1, the remainder labels indicate by which fraction this value is diminished in the simulation. Thus the response of the cell solid temperature to the efficiency of the integrated

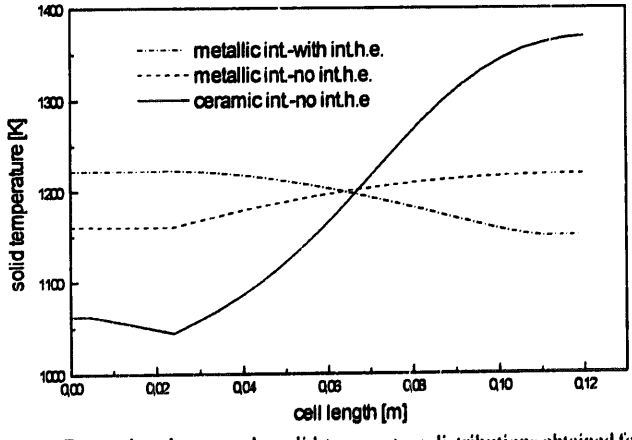

Fig. 6. Comparison between the solid-temperature distributions obtained for different cell configurations: with or without integrated heat exchanger, the latter simulated with both a ceramic and a metallic interconnector. Geometrical and operating parameters are the ones reported in Table 1 in all cases.

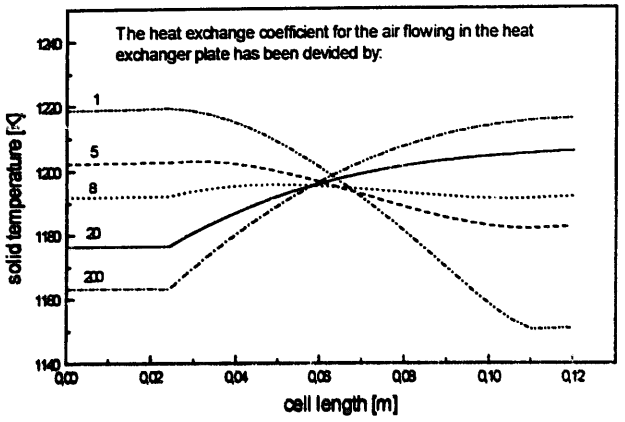

Fig. 7. Effect of variations of the heat-exchange coefficient for the air flowing into the integrated exchanger on the solid-temperature distribution.

Table 2
Design parameters and operating conditions for the simulated rectangular stack

Simulated rectangular stack	
Design parameters	
Nos. of cells	5
Operating conditions	
Current density	3000 A m^{-2}
Stack voltage	3.55 V
Pressure	1.013×10^5 Pa
Anodic inlet temperature	1173 K
Cathodic inlet temperature	797 K
Average solid temperature	1193 K
Shell temperature	1183 K
Anodic inlet composition	97%H_2 + 3%H_2O
Cathodic inlet composition	air
Hydrogen-utilisation factor	0.8
Oxygen-utilisation factor	0.3
Heat exchange	radiation + convection

heat exchanger is illustrated. For increasing label numbers the operating conditions come continuously closer to those of a cell without integrated heat exchanger.

If the heat-transfer coefficient is reduced by a factor of 8 the temperature distribution of the solid structure is almost flat. By this measure the pre-heating air is more slowly heated up and thus able to remove the large amount of waste heat in the entrance region of the electrochemically active part of the cell, where heat is mostly dissipated.

A reduction of the heat-transfer coefficient, for instance, can easily be verified by increasing the channel height of the integrated heat exchanger.

As a matter of fact this figure does point out the benefit of the integrated heat exchanger: it is sufficient to optimise the design of the integrated heat-exchanger plate to obtain a flat temperature profile. This optimisation depends on the operating conditions (i.e. the O_2-utilisation factor).

In the case of a traditional cell (i.e. without integrated heat exchanger) the only way to achieve such a result would consist of an increase in the dimensions of the gas channels that distribute fuel and oxidant to the cell plane. In this way the path of the electrons through the electrodes and the diffusion of gases would become more and more difficult, and the electrical resistance of the cell would increase. For example, if the rib side and the channel side lengths were 2×10^{-3} m instead of 1×10^{-3} m (as it is assumed in the model, Table 1), diffusion problems of the hydrogen in the electrode would take place: the PEN electrical resistance would become about three times greater [19] (PEN: positive + electrolyte + negative, i.e., anode + electrolyte + cathode).

As the interconnector and the integrated heat exchanger have an electrical resistance that is negligible with respect to the PEN one, any change in their geometry would have negligible consequences on the electrochemical performances of the cell. The optimisation of integrated heat-exchanger cells would be recommended, also for cells using only ceramic materials.

To show the advantages of the new design, and in particular the benefit obtained by means of the optimisation, a parameter study was made investigating the influence of the O_2-utilisation on the solid temperature and on the air temperature at the inlet. The results for the heat-exchanger integrated cell and the conventional cell are plotted in Figs. 8 and 9. The new design has been optimised for this comparison with respect to the heat-exchanger conditions assuming the heat-exchange coefficient to be devided by 8.

The figures show that the temperature variations along the cell increase, while the inlet temperature decreases, with increasing O_2- utilisation. As long as the temperature profile of the cell becomes flatter, the air-outlet temperature, and as a consequence the inlet one, increases with respect to the non-optimised case (Fig. 9).

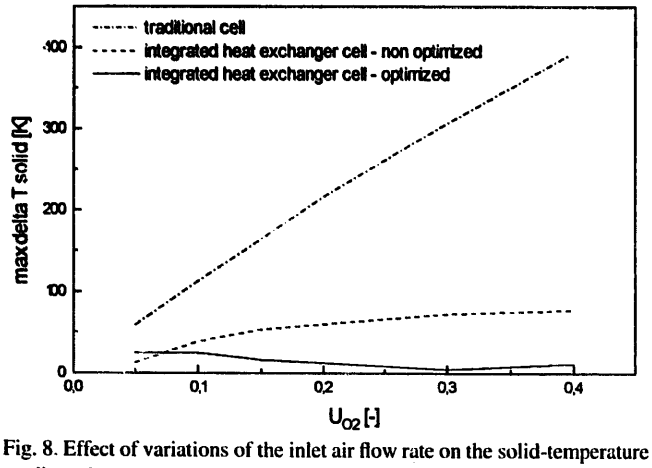

Fig. 8. Effect of variations of the inlet air flow rate on the solid-temperature gradient along the cell.

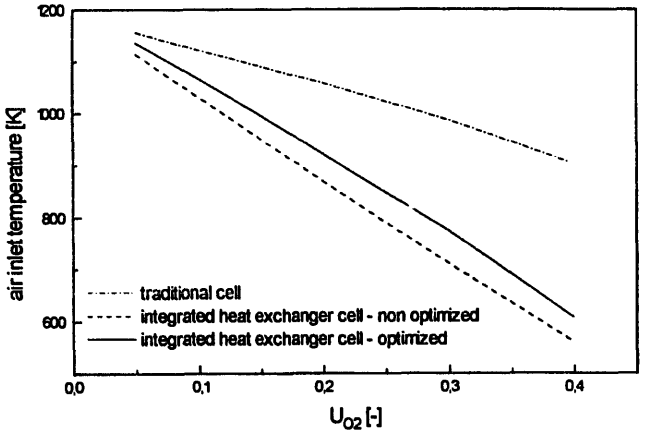

Fig. 9. Effect of variations of the inlet air flow rate on the inlet air temperature necessary to keep the average temperature of the cell at 1193 K.

3.2. *Five-cell stack*

The preceding parameter studies have been performed for a single cell which may be regarded as a centrally positioned cell in a large stack. In order to show the effect of the outer boundary conditions on the stack operation a stack consisting of five cells is considered. Details of the operating conditions are summarised in Table 2. It is assumed that the end plates radiate and convey heat to the surroundings kept at a temperature of $T_{shell} = 1183$ K.

Fig. 10 shows the temperature distribution of the solid structure along the five cells of the stack. The temperature level of the end cells is lower than that of the central cells. Since for cell 1 — in the drawing of Fig. 1 the left one — the outer channel is an air channel and for cell 5 a fuel channel, the temperature distributions of the end plates are different. The higher mass flow on the air side supplies cell 1 with heat, so that the cell temperature does not drop so much — compared with cell 5 — by the effect of radiative heat removal from the cell surface.

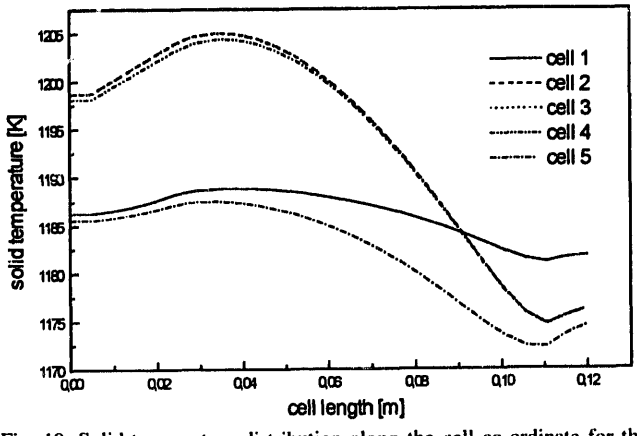

Fig. 10. Solid-temperature distribution along the cell co-ordinate for the stack.

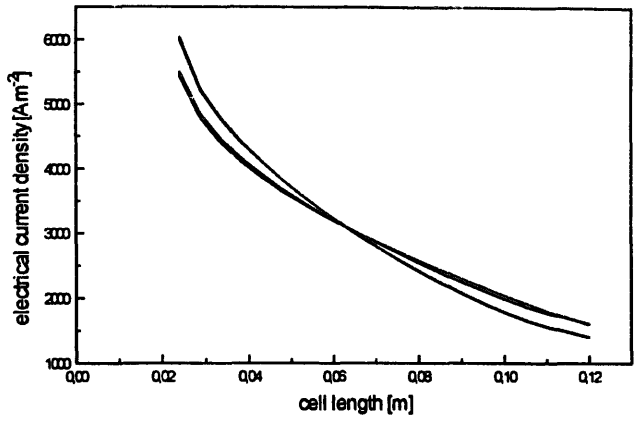

Fig. 11. Electrical current-density distribution along the cell co-ordinate for the various cells of the stack.

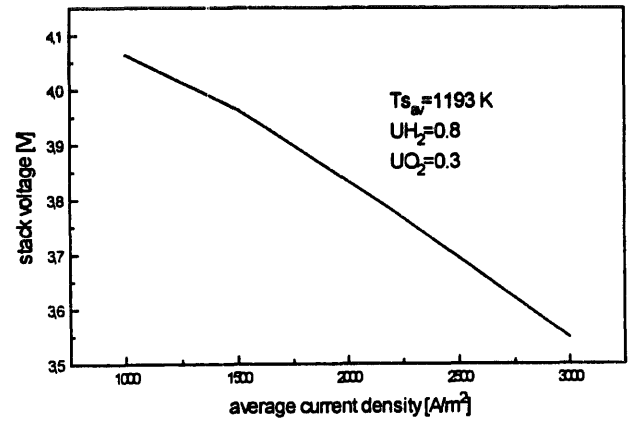

Fig. 12. Characteristic curve for the rectangular stack.

Due to the small temperature variations across the stack, only minor variations of the local current density occur between the particular cells as demonstrated in Fig. 11.

Finally, Fig. 12 represents the stack characteristic. For $j = 3000$ A m^{-2} a stack voltage of about $U = 3.6$ V is predicted corresponding to an average cell voltage of $U = 0.71$ V. The variation of this quantity along the stack is not significant.

4. Conclusions

The operating conditions of a rectangular planar SOFC with integrated air pre-heater have been analysed. The idea of this new fuel cell type is to reduce the cost of the expensive external air pre-heater by applying lower air flow rates together with lower inlet temperatures.

The parameter study indicates that the benefit increases for low air-excess rates, i.e. for high oxygen utilisation. For this case the air-inlet temperatures can drastically be reduced. The air in the pre-heater streams in counter-flow to the cathodic air and is heated up by the electrochemically produced waste heat. The high thermal conductivity of the metallic solid

structure contributes to the compensation of the temperature gradients occurring along the cell. Thus, the heat produced in the entrance region of the cell is conducted to the exit location where it is removed by the low temperature inlet air.

5. List of symbols

a	channel thickness, m
B	ratio gas–solid heat-exchange area/cell area, –
C_p	massic specific heat, J kg^{-1} K^{-1}
c_p	molar specific heat, J mol^{-1} K^{-1}
d_h	hydraulic diameter, m
e	emissivity, –
E	activation energy, J mol^{-1}
F	Faraday constant, A s mol^{-1}
h	heat-transfer coefficient, W m^{-2} K^{-1}
I	electrical current density, A m^{-2}
k	gas heat conductivity, W m^{-1} K^{-1}
K	solid heat conductivity, W m^{-1} K^{-1}
n	molar flow rate, mol m^{-2} s^{-1}
ne	number of electrons transferred in the reaction, –
p	partial pressure, Pa
p_{ref}	reference pressure, Pa
q	heat flux, W m^{-2}
R	gas constant, J mol^{-1} K^{-1}
r	reaction rate, mol m^{-3} s^{-1}
R_{el}	electrical resistivity, Ω m
R_{pol}	polarization resistance, Ω m^2
s	cell thickness, m
t	time, s
T	temperature, K
x, z	length co-ordinates, m
V	potential, V

Greek letters

α	heat-transfer coefficient between stack and shell, W m^{-2} K^{-1}
β_1, β_2, β_3	coefficients defined in Eq. (9), Ω K m^{-1}, –, K
δ	thickness, m
ΔH	enthalpy change of the over-all reaction, J mol^{-1}
ΔG	Gibbs free energy change of the over-all reaction, J mol^{-1}
ΔG^0	standard Gibbs free energy change of the over-all reaction, J mol^{-1}
γ_1, γ_2	coefficients defined in Eqs. (10), (11), A m^{-2}, –
λ	stoichiometry factor, –
ν	stoichiometric coefficient, –
ρ	density, kg m^{-3}
σ	constant of Stefan–Boltzman, W m^{-2} K^{-4}

Subscripts

an	anode
av	average
ca	cathode
g	gas
h	layer
i	chemical species
s	solid
shell	shell
x	x-direction
z	z-direction

Superscripts

oc	open circuit
cc	current collectors
ohm	ohmic effects
pol	polarization effects

Acknowledgements

The author wish to thank KFA Jülich, where she began the work, and in particular Professor. E. Achenbach for his valuable help.

References

[1] J.H. Hirschenhofer, D.B. Stauffer and R.R. Engleman, *Fuel Cells, A Handbook (Revision 3), DOE/METC-94/1006 (DE94004072)*, US Department of Fossil Energy, Morgantown Energy Technology Center, Morgantown, WV, USA, 1994.

[2] E. Achenbach, R. Riensche and G. Unverzagt, *Proc. 1st European Solid Oxide Fuel Cell Forum, Lucerne, Switzerland, Oct. 1994*, p. 153.

[3] H. Ringel, *KFA Jülich ZAT-Bericht 281-II.4-12*, Sept. 1994.

[4] R. Diethelm, K. Honegger and E. Batawi, *Proc. 1st European Solid Oxide Fuel Cell Forum, Lucerne, Switzerland, Oct. 1994*, p. 947.

[5] C.G. Vayenas, P.G. Debenedetti, I. Yentekakis and L.L. Hegedus, *Ind. Eng. Chem. Fundam., 24* (1985) 316.

[6] R. Selman, R. Herbin, M. Flück and R. Gruber, *Proc. IEA SOFC Workshop, Hertenstain, Switzerland, June 1990*, p. 17.

[7] E. Erdle, J. Großß, H.G. Müller, W.J.C. Müller, H.J. Reusch and R. Sonnenschein, *Proc. 2nd Int. Symp. Solid Oxide Fuel Cells, Athens, Greece, July 1991*, p. 265.

[8] P. Costa, E. Arato, L. Maga and O. Paladino, *Chem. Biochem. Eng. Q., 5* (1991) 43.

[9] E. Arato and P. Costa, *Chem. Biochem. Eng. Q., 7* (1993) 161.

[10] E. Arato and P. Costa, *SOFC Stack Design Tool, An Int. Energy Agency SOFC Task Rep., Berne, Switzerland, Nov. 1992*, p. 6.

[11] M. Østenstad, *SOFC Stack Design Tool, An Int. Energy Agency SOFC Task Rep., Berne, Nov. 1992*, p. 18.

[12] J.R. Ferguson, *SOFC Stack Design Tool, An Int. Energy Agency SOFC Task Rep., Berne, November 1992*, 31.

[13] J.M. Fiard and R. Herbin, *SOFC Stack Design Tool, An Int. Energy Agency SOFC Task Rep., Berne, Nov. 1992*, p. 50.

[14] K. Nisancioglu, *Proc. 5th IEA Workshop on SOFC, Jülich, Germany, Mar. 1993*, p. 113.
[15] O. Melhus, *Proc. 5th IEA Workshop on SOFC, Jülich, Germany, Mar. 1993*, p. 263.
[16] Ch. Rechenauer and E. Achenbach, Dreidimensionale mathematische Modellierung des stationären und instationären Verhaltens oxidkeramischer Hochtemperatur-Brenn-stoffzellen. *Jül Rep. 2752*, Apr. 1993.
[17] E. Achenbach, *J. Power Sources, 49* (1994) 333.
[18] U. Bossel, Facts and figures, *IEA Task Rep., Berne, Apr. 1992*.
[19] P. Costamagna and E. Arato, *Proc. 1st European Solid Oxide Fuel Cell Forum, Lucerne, Switzerland, Oct. 1994*, p. 287.